Growth of Titanium Dioxide Nanorods in 3D-Confined Spaces
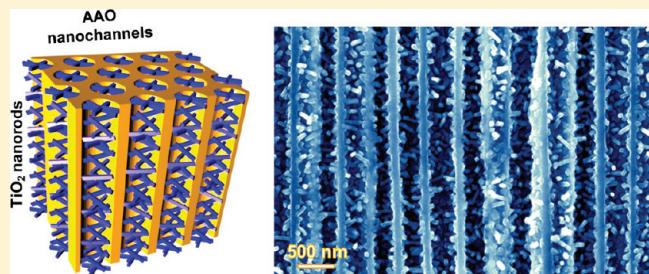
Jian Shi, Chengliang Sun, Matthew B. Starr, and Xudong Wang*

Department of Materials Science and Engineering, University of Wisconsin—Madison, Madison, Wisconsin 53706, United States

Ⓢ Supporting Information

ABSTRACT: Three-dimensional (3D) nanowire (NW) networks are promising architectures for effectively translating the extraordinary properties of one-dimensional objects into a 3D space. However, to uniformly grow NWs in a 3D confined space is a serious challenge due to the coupling between crystal growth and precursor concentration that is often dictated by the mass flow characteristic of vapor or liquid phase reactants within the high-aspect ratio submicrometer channels in current strategies. We report a pulsed chemical vapor deposition (CVD) process that successfully addressed this issue and grew TiO_2 nanorods uniformly covering the entire inner surface of highly confined nanochannels. We propose a mechanism for the anisotropic growth of anatase TiO_2 based on the surface-reaction-limited CVD process. This strategy would lead to the realization of NW-based 3D nanoarchitectures from various functional materials for the applications of sensors, solar cells, catalysts, energy storage systems, and so forth.

KEYWORDS: Pulsed CVD, titanium dioxide, nanorod

Over the past two decades there have been significant advances in the development of one-dimensional (1D) nanostructures.[1-4] The wire-like geometry not only introduces remarkably enlarged and well-defined crystal surfaces over planar structures but also provides 1D confined channels which could fundamentally tailor the transportation of electrons, phonons, and photons.[5-8] Fully capturing the promising surface and transport properties in practical devices or systems relies on the capability of effectively translating the extraordinary 1D characteristics into the three-dimensional (3D) space.[9-12] For instance, 3D electronics made by sequential printing of nanowire (NW) arrays have demonstrated substantial advantages in power consumption, integration density, and operation speed over their two-dimensional (2D) counterparts.[13-15] Photovoltaic devices fabricated by aligned or partially aligned NW array configurations have exhibited enhanced performance owing to improved carrier collection, reduced optical reflection, and efficient absorption.[16-28]

Current techniques for growing single-crystalline NWs from bottom up all rely on precipitation of precursors.[3,4,29,30] Next generation devices will most likely require precise material chemistry in engineered 3D architectures. To date, however, to synthesize such a 3D NW array inside a highly confined space is very challenging, particularly when this space is compatible to the size of the NW itself. Due to the nonuniform distribution of precursors within the confined diffusion channels, uniform growth of NWs inside such channels is extremely difficult. Among all bottom-up nanostructure synthesis techniques, atomic layer deposition (ALD) is one excellent approach that produces conformal coating in high aspect ratio channels owing to its self-limiting surface reaction.[31-33] ALD has been widely applied to grow conformal thin film coating with precisely controlled thickness down to the subnanometer level.[31,34-36] A recent discovery has also shown that introducing metal catalysts to the ALD process could lead to the transition from conformal coating to vapor—liquid—solid growth of NW morphology.[37]

In this paper, we mimic the ALD process using separated exposures of gaseous $TiCl_4$ and H_2O precursors at high temperature and extended pulsing and purging times. Through this approach, titanium dioxide (TiO_2) nanorod (NR) arrays were successfully grown uniformly along the entire inner surface of highly confined nanochannels. Control experiments suggested that the growth of TiO_2 NRs might undergo a surface-reaction-limited chemical vapor deposition (CVD) process, and this synthesis approach is thus considered as pulsed CVD. Due to the promising application potential in the field of catalysis and renewable energy,[38-44] TiO_2 thin film ALD has been intensively studied.[45-50] However, to our best knowledge, this is the first strategy for successfully growing a 3D TiO_2 NR network architecture in highly confined spaces, which might also be applied to a variety of other functional materials.

Growth of TiO_2 NRs was performed in a homemade ALD system at 600 °C using $TiCl_4$ and H_2O as precursors and anodic aluminum oxide (AAO) membrane as a deposition substrate. Two stainless steel tubes that connect two precursor containers, respectively, were plugged into the furnace chamber separately to prevent the mixing and reaction of $TiCl_4$ and H_2O before they
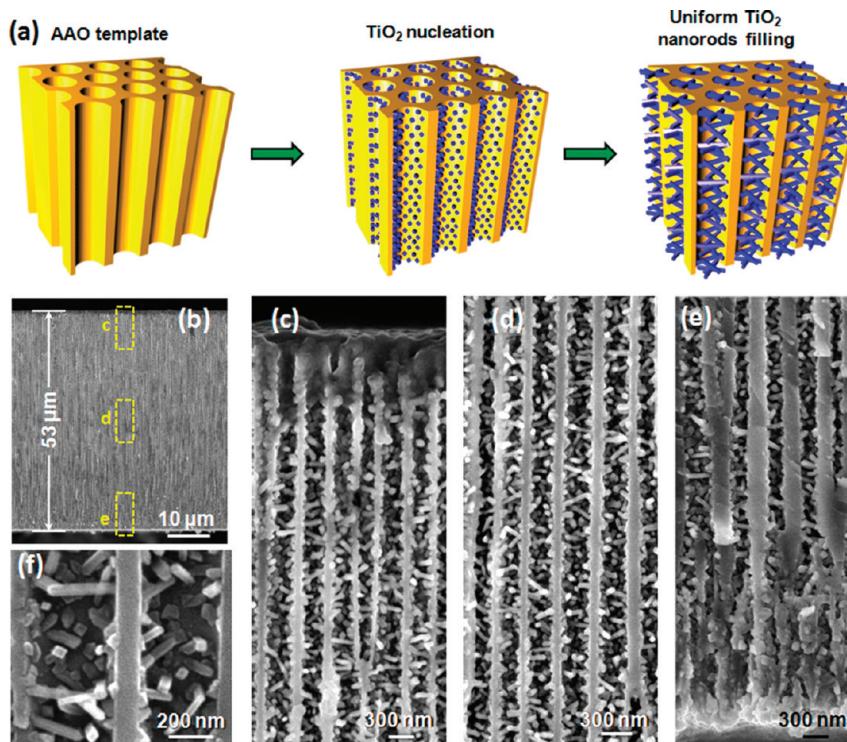
Figure 1. TiO$_2$ NRs grown in nanochannels. (a) Schematic presentation of the pulsed CVD growth inside an AAO template, where TiO$_2$ NRs can be uniformly grown along the entire inner channel walls. (b) Overview of a cross section of the AAO template after 660 growth cycles. (c−e) Higher-magnification SEM images showing the uniform and dense coating of TiO$_2$ NRs within the AAO channels at the top, middle, and bottom sections, respectively, as indicated by the dashed yellow boxes in (b). (f) TiO$_2$ NRs rooted on the walls of AAO channels showing a squarelike cross section and well-faceted shape.

were injected into the chamber. The AAO substrate was supported by a hemicylindrical quartz boat (thus 5 mm open space was left under the back side of the AAO) and placed at the center of the stainless steel tube chamber, 10 cm downstream from the precursor gas inlet. During the growth, a constant flow of 40 sccm nitrogen (N$_2$) was applied into the chamber as the carrier gas. With the flow of N$_2$ gas, the total pressure was 300 mTorr (40 Pa). The chamber temperature was maintained at 600 °C. TiCl$_4$ and H$_2$O vapor precursors were pulsed into the chamber for 1.5 s each and separated by N$_2$ purging for 60 s. One complete growth cycle includes 1.5 s of H$_2$O pulse + 60 s of N$_2$ purging + 1.5 s of TiCl$_4$ pulsing + 60 s of N$_2$ purging. After growth, the chamber cooled down to room temperature naturally (typically taking several hours) with N$_2$ flow. It was found that the extended pulsing and purging times and high temperature were critical for the formation of TiO$_2$ NR morphology.

Figure 1a schematically illustrates the growth of TiO$_2$ NRs. Starting from an AAO template with ultralong and narrow channels, this process produces TiO$_2$ nanocrystallites that uniformly cover the entire inner surface of the AAO channels. Under desired conditions, these nanoparticles (NPs) will continuously grow into NRs, which protrude radially inward. The AAO templates used in our experiments were ∼53−54 μm thick with the channel diameter of ∼250 nm, which yields an aspect ratio of ∼200 (Figure S1, Supporting Information). Figure 1b shows the cross section of the AAO template after 660 cycles of pulsing and purging. Scanning electron microscopy (SEM) images acquired from the top, middle and bottom section are shown in panels c, d, and e of Figure 1, respectively, revealing the uniform and dense coverage of TiO$_2$ NRs along the entire channel length except the

1−2 μm entrance regions. Closer examination shows that all NRs were rooted on the walls of the AAO channels and pointed inward (Figure 1f). Most NRs exhibit a rectangular cross section with a few tens of nanometers in width and a few hundred nanometers in length. The length and width distributions were statistically analyzed along the channels (Figure S2, Supporting Information). The majority of the as-synthesized TiO$_2$ NRs had lengths and widths of between 170 and 210 nm and 25 and 30 nm, respectively. The narrow NR size distribution across the entire channel length indicates an effectively decoupling of the crystal growth from the precursor partial pressure. The anatase phase of the TiO$_2$ NRs was initially identified by X-ray diffraction (XRD) and the composition was confirmed by energy-dispersive X-ray spectroscopy (EDS) (Figure S3, Supporting Information).

To investigate the growth behavior of TiO$_2$ NRs inside the AAO channel, growth cycles of 85, 170, 330, 660, 900, and 1200 were applied and the evolution of NR morphology was examined by SEM (Figure 2a). Length and width measurements revealed a faster growth rate in the first several hundred cycles (Figure 2b). Before the 330-cycle growth point, the average growth rate along the length was ∼0.5 nm/cycle, while subsequent rate dropped to ∼0.1 nm/cycle. Growth rate along the width direction was ∼0.03 nm/cycle. The slower growth rate was possibly the consequence of less volume left in the AAO channel for precursor transportation when the sizes of NRs became larger. The length of the NRs saturated at 230−240 nm which correlated with the average diameter of the AAO channels (∼250 nm). The aspect ratio of NRs followed a parabola-like curve, increasing from 1 (at 85 cycles) to a maximum of 7 (at 900 cycles) (Figure 2c).
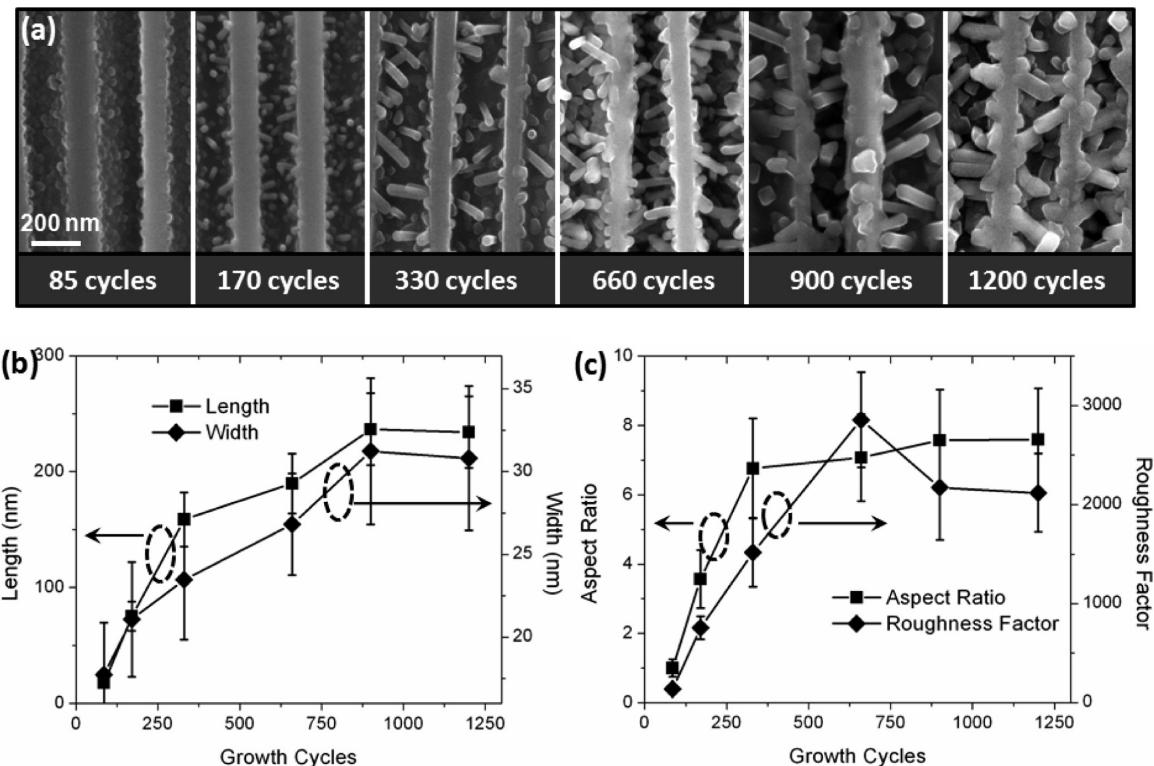
Figure 2. Growth rate and evolution of TiO$_2$ NR structures. (a) SEM images of typical NR morphology after different growth cycles. From left to right are 85, 170, 330, 660, 900, and 1200 cycle results. (b) Plots of NR length (square symbol) and thickness (diamond symbol) vs growth cycles. The data were collected from several hundred NR samples. (c) Plots of aspect ratio of NRs (square symbol) and roughness factor (diamond symbol) vs growth cycles. The highest aspect ratio was ∼7 at 900 cycles. The maximum value of roughness factor reached ∼3000 at 660 cycles.

The slight decrease of aspect ratio after 900 cycles was a consequence of the saturation of NR length.

Further statistical study revealed a fairly uniform NR geometry distribution inside the AAO channel (Figure S4, Supporting Information). The growth rate of the NR width was ∼0.3−0.4 Å/cycle (∼0.15−0.2 Å/cycle on each side), which was about a quarter of the typical amorphous TiO$_2$ film ALD deposition rate (0.8 Å/cycle). On the other hand, the growth rate along the NR length direction was ∼5 Å/cycle, which was more than 6 times higher than the typical ALD film growth rate. Such an anisotropic growth behavior is different from the ALD and could be the key to understand the NR growth mechanism.

Such a NR 3D architecture offered a very high surface area. The roughness factor, which is defined as the total NR surface area per unit substrate area, reached ∼3000 (cal.) at 660 cycles. This number is about the same as the roughness factor of highly packed NP networks and nearly 10 times higher than pure NW arrays with the same vertical length. The high roughness factor suggests that our approach would enable a novel and high-performance 3D electrode architecture for photovoltaic or catalytic cells, when the TiO$_2$ NRs are grown inside a conductive nanoskeleton.

A series of controlled experiments was performed to understand the NR growth via the pulsed CVD process. The observation that only NP morphology was found on the surface of the AAO template suggested that nanochannels might be a favorable geometry for anisotropic growth (Figure S5a, Supporting Information). In addition, transmission electron microscopy (TEM) analysis shows that those NPs were constructed by the {011} surfaces (Figure S5b,c, Supporting Information), which were

later found to have different exposed facets from TiO$_2$ NRs. Through the same process (660 cycles, 1.5 s pulse time, and 60 s purge time), NPs were found to be the dominant morphology on the surface of polycrystalline Al$_2$O$_3$ (Figure S6a, Supporting Information), exposed AAO channel surface (Figure S6b, Supporting Information), and Si substrate (Figure 3a-i). The low precursor partial pressure inside the confined AAO channels might be a reason for formation of NR structure. In order to test this hypothesis, a reduced pulsing time (200 ms) was applied to grow TiO$_2$ on a flat silicon substrate. From the pressure gauge readouts, the 200 ms pulsing time could reduce the precursor partial pressure by ∼75% compared to the 1.5 s pulsing time. After 330 cycles, scattered NR morphology was observed (Figure 3a-ii), which indicates that the partial pressure is one of the parameters that control the formation of NR morphology. However, these NRs were smaller than those collected inside AAO channels. Therefore, it is reasonable to conclude that the longer dwelling time of precursor molecules inside AAO channels would lead to larger size of NRs. The AAO channels could not only reduce the precursor partial pressure to a proper level favoring the NR growth but also act as a reservoir for continuously supplying precursors for a longer time.

A series of experiments were conducted to test the purging time effect as shown in Figure 3b. The shorter purging time (5 and 20 s at 330 cycles) resulted in the formation of NPs inside the AAO channels, while sparse small NRs morphology can be found in the 20 s sample (Figure 3b-ii). NR morphology appeared when the purging time increased to 1 min (Figure 3b-iii). These observations suggest that a short purging time might not be sufficient to complete the surface CVD reactions or to demonstrate
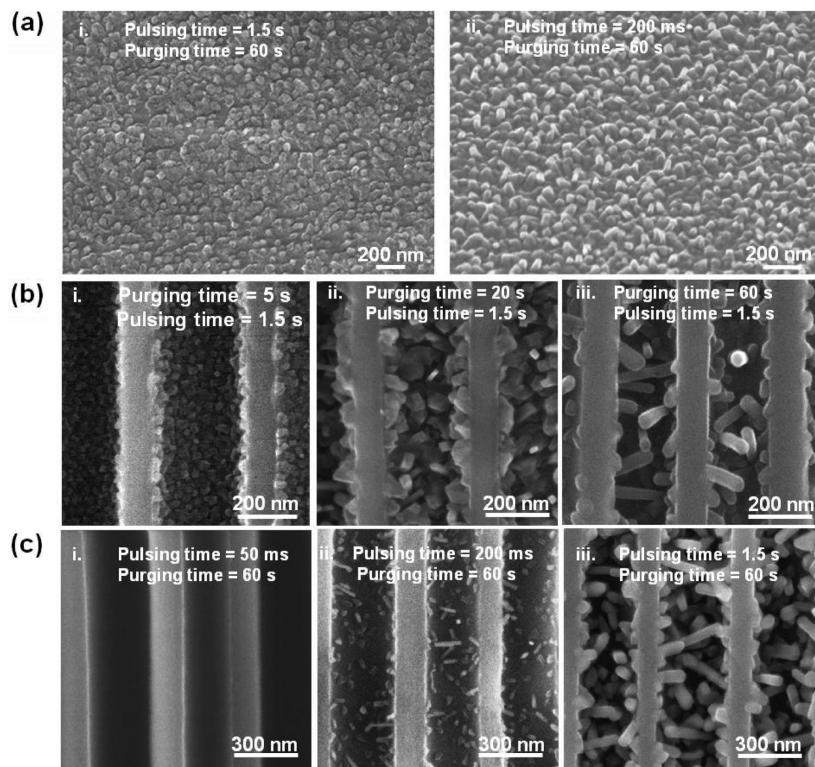
Figure 3. Anatase TiO_2 nanostructures deposited under controlled experimental conditions. (a) Exposure time effect on flat silicon substrate using 330 growth cycles at 600 °C and 60 s purging time: (i) NPs were received with regular pulsing time (1.5 s); (ii) NR morphology started to develop with reduced pulsing time (200 ms). (b) Purging time effect on TiO_2 morphology using 330 growth cycles at 600 °C and 1.5 s pulsing time: (i) NPs were received with 5 s purging time; (ii) majority NPs were received with 20 s purging time, but sparse small NRs can be found; (iii) dominating NR morphology received with 60 s purging time. (c) Pulsing time effect on TiO_2 morphology using 330 growth cycles at 600 °C and 60 s purging time: (i) no deposition was observed with 50 ms pulsing time; (ii) low density and tiny TiO_2 NRs were found with 200 ms pulsing time; (iii) regular size TiO_2 NRs were received with 1.5 s pulsing time.

the different growth behaviors of different crystal surfaces. We believe longer purging time would be necessary to preferentially remove physically absorbed precursor molecules from certain crystal surfaces thus to facilitate the anisotropic growth. These findings demonstrated a reasonable direction for applying pulsed CVD-based NR growth technique to a variety of substrates and surface features.

The effect of pulsing time was also studied inside the AAO channels (Figure 3c), where 50 ms, 200 ms and 1.5 s pulsing times were applied to grow TiO_2 NRs with the same 60 s purging time and 660 growth cycles. The 200 ms pulsing time resulted in much smaller (~10 nm in width and ~50 nm in length) and less dense NRs than those produced by 1.5 s pulsing time. No deposition was obtained when the pulsing time was reduced to 50 ms. Considering that the ALD TiO_2 film could be fabricated at 80 °C with a 50 ms pulsing time and 60 s purging time in our system, the absence of deposition at 600 °C indicates that a nucleation event may not be able to occur when the precursor partial pressure is too low. The low density of tiny TiO_2 NRs grown in AAO channels with a pulsing time of 200 ms implies that low partial pressure would lead to a small number of nucleations. The pulsing-time-dependent NR growth is consistent with typical CVD growth behavior. It should be noted that the initial nucleation of the NRs is still uncertain at this point. Further understanding of the nucleation would be essential for applying this technique to different substrates and material systems.

The TiO_2 NRs assemblage and morphology were further characterized by TEM. Figure 4a shows a cross section of the AAO channels crisscrossed with TiO_2 NRs. The compact NR arrays were found evenly distributed inside the AAO channel. In order to investigate the adhesion between neighboring NRs, the AAO templates were removed by immersing the samples in a mild phosphoric acid solution for 5 h at 80 °C. Below 660 cycles, most tubular NRs assemblages fell apart after template removal, indicating isolated growth sites of the NRs. However, if the growth was increased from 660 to 1200 cycles, tubular assemblages were observed post AAO template removal (Figure 4b). This observation suggested that the additional crystal growth was sufficient to physically interlink the NR roots together.

A typical TiO_2 NR morphology (growth >300 cycles) is shown in Figure 4c, where the NR exhibited a highly uniform thickness, well-faceted surfaces, and an aspect ratio of ~7. Uniform contrast was observed on the corresponding dark field image (Figure 4d), indicating the high lattice quality and a dislocation-free structure. Selected area electron diffraction (SAED) taken on the NR further confirmed the anatase structure (inset of Figure 4e and Figure S7, Supporting Information) with the {011} as side surfaces and the {100} as the surfaces in-plane of the image. Combination of the [002] and [0$\bar{1}$1] directions was identified as the NR growth direction. High-resolution TEM (HRTEM) clearly revealed the arrangement of the (002) and (0$\bar{1}$1) planes along the NR growth direction with a lattice spacing of 0.48 and 0.35 nm, respectively (Figure 4e). Such a lattice
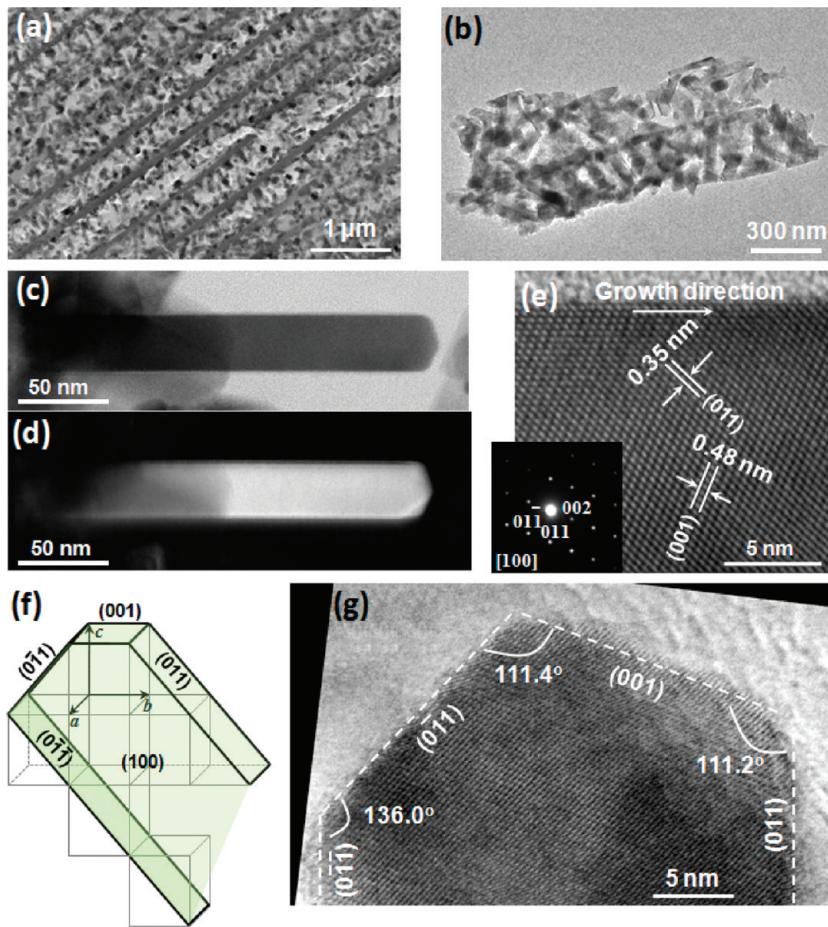
Figure 4. Structure and morphology characterizations of TiO$_2$ NRs. (a) TEM image of a cross section of AAO channels filled with TiO$_2$ NRs grown by 660 cycles. (b) TiO$_2$ NR bundles after dissolving the AAO template completely, where the growth cycle is 1200. (c, d) Bright field and dark field TEM images of a single-crystalline TiO$_2$ NR demonstrating high thickness/width uniformity and excellent crystal integrity. (e) High-resolution TEM image of an anatase TiO$_2$ NR. Measured lattice spacing of the (011) and (002) planes are 0.35 and 0.48 nm, respectively. Inset is the corresponding selective-area diffraction (SAED) pattern. (f) Proposed TiO$_2$ NR structure shaped by three groups of atomic planes: {100}, {011}, and {001}. A unit cell is represented by a cube with a, b, and c parallel to the [100], [010], and [001] directions, respectively. (g) HRTEM image of a typical NW tip faceted by the (001), (011), (01̄1̄), and (01̄1) planes. The asymmetric tip geometry is the result of different crystal surface areas and different interplanar angles.

orientation represented all anatase NRs characterized by TEM. On the basis of the SEM, SAED, and TEM observations, the structure of an anatase NR is illustrated in Figure 4f. The four side planes of a NR are (011), (01̄1̄), (100), and (1̄00). They are perpendicular to each other and form a rectangular cross section. The top surface of the NR is composed of the (001) and (01̄1) planes. From the HRTEM image of a NR tip (Figure 4g), the angle of the tip was observed to be 111.4°, which is consistent with the angle between the (001) and (01̄1) planes. These two planes often exhibited different surface areas, resulting in an asymmetrical NR tip. Such a growth orientation is different from the anatase TiO$_2$ NWs synthesized by hydrothermal or vapor deposition processes, where the growth direction is along the ⟨011⟩ or the ⟨001⟩ and the commonly observed facets of anatase TiO$_2$ are {011} or {101} due to their low surface free energy as predicted by theoretical calculations.[19,43,51−55]

Further HRTEM characterization revealed that all the TiO$_2$ NRs exhibited atomically flat {011} surfaces (Figures 4g and S8a, Supporting Information), while the (001) plane was marked by islands and multiple atomic steps (Figures 4g and S8b, Supporting Information). Such unevenness of the NR tip could also be observed along the [100] direction (Figure S9, Supporting Information).

At the early growth stage (330 cycles or less), TiO$_2$ NRs often exhibited a nonfaceted or irregular tip, but the atomically flat side surfaces could already be clearly observed (Figure S10, Supporting Information). These observations suggest that the (001) plane was a particularly active deposition and growth surface. In a rare case, planar defects were observed along the (001) surface (Figure S11, Supporting Information), which would also be a consequence of fast growth of the (001) planes. However, the observed growth was along a high-index orientation which was close to the [01̄5] direction. This disparity may be a result of the nonorthogonality of the fast growing (001) plane with respect to the slower growing {011} and {100} side planes.

Beginning with the observation that the (001) surface was the dominant and active growth front, we analyzed and compared the (001) plane with the {011} and {100} planes and propose a model to explain why the (001) plane exhibited a significantly faster growth rate compared to other planes in the pulsed CVD process. Figure 5a shows the crystal structure of anatase TiO$_2$ represented by a 2 × 2 × 2 supercell, where the {001}, {011}, and {100} facets are highlighted in purple, green, and yellow, respectively. Cleavage surfaces along these planes are shown in Figure 5b. Each plane includes one randomly selected Ti atom
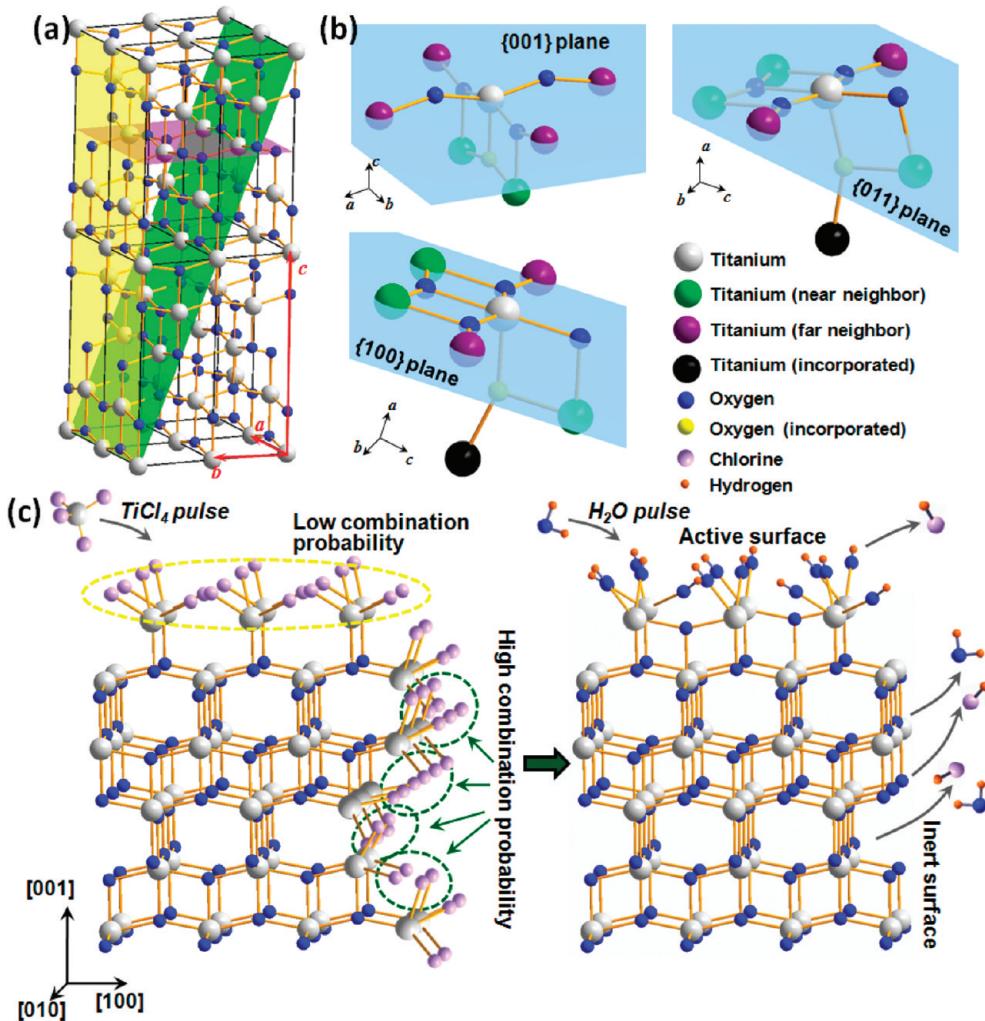
Figure 5. Understanding the TiO$_2$ NR growth mechanism. (a) Crystal structure model of a $2 \times 2 \times 2$ supercell of anatase TiO$_2$, where the (001), (011), and (100) planes are highlighted by purple, green, and yellow, respectively. (b) Ball-and-stick model of the {001}, {011}, and {100} cleavage surfaces centered with a randomly selected Ti atom (gray). Green and purple Ti atoms represent the near and far neighbors, respectively, in corresponding to the center Ti atom. Incorporated Ti (black) is inside the lattice and chemically inert. The {001} surface has three far and one near neighboring Ti atoms, while the {011} and {100} surfaces have one far and three near neighboring Ti atoms. (c) Schematic illustration of one ideal pulsed CVD growth cycle. The left-hand-side shows the (001) and (100) planes after a TiCl$_4$ pulse. For clear presentation, we assume all the surface Ti atoms on the (001) and (100) planes are newly added during the TiCl$_4$ pulse. Thus, each of them has three Cl attached. The right-hand-side shows the situation after following water pulse. The (100) surface becomes inert due to the near-neighbor self-combination, while the (001) surface remains active with the Cl replaced by $-$OH groups. The {011} planes (not shown) would have the same property as the {100} planes.

Table 1. The Number of Far-Neighbor or near-Neighbor Ti Atoms with Respect to a Randomly Selected Center Ti Atom[a]

atomic plane	number of far neighbors	number of near neighbors
{001}	$1/2 \times 2 + 1 \times 2 = 3$	$1/2 \times 2 = 1$
{100}	$1/2 \times 2 = 1$	$1 + 1/2 \times 4 = 3$
{011}	$1/2 \times 2 = 1$	$1 + 1/2 \times 4 = 3$

[a] The number is counted based on oxygen sharing. If one neighbor shares one oxygen exclusively with the selected Ti atom, it is counted as 1; if two neighbors share one oxygen together with the selected Ti atom, each is counted as 1/2.
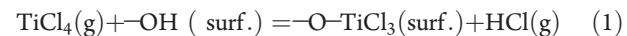
(colored with white) and all of its neighboring Ti atoms which can bond with the selected Ti through an intermediate O atom (blue). Three types of neighboring Ti atoms can be classified:

(1) Incorporated Ti atom (black). This Ti atom lies inside the crystal lattice and is chemically inert. It is considered as the atom that previously provided the chemical bonding site to a TiCl$_4$ molecule and captured it onto the surface.
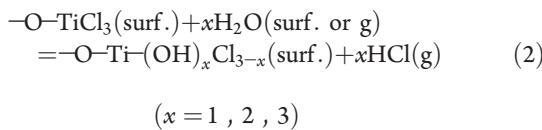
(2) Far-neighbor (purple). A Ti atom that is 3.78 Å away from the center Ti atom.

(3) Near-neighbor (green). A Ti atom that is 3.04 Å away from the center Ti atom.[56]

The numbers of Ti neighbors on different atomic planes, and their relationships to one another, are summarized in Table 1. In a pulsed CVD process, when TiCl$_4$ molecules diffuse onto the growth front, they could incorporate into the TiO$_2$ lattice through the chemical reaction with surface $-$OH groups, as shown in eq 1.

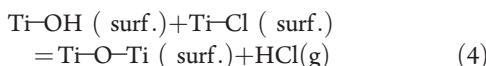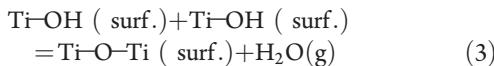$$TiCl_4(g) + -OH \ (surf.) = -O-TiCl_3(surf.) + HCl(g) \quad (1)$$

The Cl on the $-$TiCl$_3$ group are active atoms that will react with the absorbed H$_2$O molecules (if there are any) within the same

cycle or the H_2O precursor during the next pulse, as shown in eq 2.

$$-O-TiCl_3(\text{surf.})+xH_2O(\text{surf. or g})$$
$$=-O-Ti-(OH)_xCl_{3-x}(\text{surf.})+xHCl(g) \qquad (2)$$

$$(x = 1, 2, 3)$$

The $-OH$ groups are active groups that can react either of two ways: with other surface active atoms (self-combination—a termination process, as shown in eqs 3 and 4) or with the $TiCl_4$ precursor molecules (eq 1).

$$\text{Ti}-\text{OH (surf.)}+\text{Ti}-\text{OH (surf.)}$$
$$=\text{Ti}-\text{O}-\text{Ti (surf.)}+H_2O(g) \qquad (3)$$

$$\text{Ti}-\text{OH (surf.)}+\text{Ti}-\text{Cl (surf.)}$$
$$=\text{Ti}-\text{O}-\text{Ti (surf.)}+HCl(g) \qquad (4)$$

If all $-OH$ or $-Cl$ groups on a Ti atom are replaced by the $-O-Ti-$ bonds, this Ti atom is regarded as inactive. We assume that the possibility of self-combination between near neighbors would be significantly higher than that between far neighbors. Thus, during a long purging time ($\sim$60 s) at sufficiently high temperature ($\sim$600 °C), the system approaches the limit where all near neighbors have undergone self-combination with one another but some of the far neighbors still remain active. On the basis of this rationale, the {100} and {011} surfaces would become an inert surface before the following $TiCl_4$ pulse, because of the existence of three near neighbors, which would consume all active $-OH$ groups by self-combination. Therefore, these two surfaces might not be favorable for absorbing precursor molecules for surface chemical reactions during both the pulsing and purging stage. However, the {001} surface would maintain its chemical activity due to the existence of only one near neighbor. The large number of active functional groups would allow strong absorption and quick reaction of precursor molecules on this surface.

Figure 5c schematically illustrates the growth fronts at the (001) and (100) surfaces in such an ideal case, where the surfaces are covered by $-TiCl_3$ active groups after the $TiCl_4$ pulse. During the H_2O pulsing and following purging periods at high temperature, the $-Cl$ atoms will react with H_2O. On the (100) surface, the majority of $-TiCl_3$ groups become inactive due to the self-combination among near neighbors. The (001) surface, however, is dominated by far neighbors. Thus, the self-combination probability is much lower on this surface, leaving a significant amount of actively surface $-OH$ groups that could effectively absorb the unreacted $TiCl_4$ and H_2O molecules. The active surface and sufficient absorbed precursors make the chemical reaction rate faster on the (001) surface than on the inert {011} or {100} surfaces.

Therefore, the TiO_2 NR was grown by rapid surface chemical reaction on the active (001) planes but growth-limited to an equal degree on the inert {100} and {011} facets. This mechanism explains the observed growth rate difference along the different crystal planes for NR growth. When the partial pressures of both precursors are sufficiently high, such as the condition shown in Figure 3a-i, the difference of the molecule absorption abilities between the {001} and {011} or {100} might become trivial and NP morphology was formed. When the purging time was not long enough, such as the conditions shown in Figures 3, panels b-i and ii, the physically adsorbed precursor molecules might not be effectively removed from the inert {011} and {100} surfaces,

and thus NP morphology was more likely to appear. Since NR growth was found to be limited by the precursor absorption and surface chemical reaction, this approach was suggested as the surface-reaction-limited pulsed CVD process.

In summary, single-crystalline anatase TiO_2 NR arrays were grown uniformly covering the entire inner surface of highly confined nanochannels by a surface-reaction-limited pulsed CVD approach. This technique applied separated exposures of gaseous $TiCl_4$ and H_2O precursors. The anisotropic growth of TiO_2 crystal is believed to be the result of the combined effects of the surface-related precursor molecule absorption and reaction. The (001) surface of TiO_2 crystal has also been found to be essential for the formation of NR morphology. Further in-depth understanding of the nucleation step is greatly desired for fully revealing the NR formation process. Understandings established on this surface reaction-limited CVD of TiO_2 NRs would eventually allow us to realize a NW-based 3D nanoarchitecture from a variety of functional materials for the applications of sensors, solar cells, catalysts, energy storage systems, and so forth.

■ ASSOCIATED CONTENT

ⓢ **Supporting Information.** Additional figures showing SEM images, nanorod distribution, and XRD spectra. This material is available free of charge via the Internet at http://pubs.acs.org.

■ AUTHOR INFORMATION

Corresponding Author
*E-mail: xudong@engr.wisc.edu.

■ ACKNOWLEDGMENT

■ REFERENCES

(1) Kuchibhatla, S. V. N. T.; Karakoti, A. S.; Bera, D.; Seal, S. *Prog. Mater. Sci.* **2007**, *52* (5), 699–913.

(2) Lieber, C. M. *Solid State Commun.* **1998**, *107* (11), 607–616.

(3) Xia, Y. N.; Yang, P. D.; Sun, Y. G.; Wu, Y. Y.; Mayers, B.; Gates, B.; Yin, Y. D.; Kim, F.; Yan, Y. Q. *Adv. Mater.* **2003**, *15* (5), 353–389.

(4) Barth, S.; Hernandez-Ramirez, F.; Holmes, J. D.; Romano-Rodriguez, A. *Prog. Mater. Sci.* **2010**, *55* (6), 563–627.

(5) Tian, B.; Kempa, T. J.; Lieber, C. M. *Chem. Soc. Rev.* **2009**, *38* (1), 16–24.

(6) Lieber, C. M.; Wang, Z. L. *MRS Bull.* **2007**, *32* (2), 99–108.

(7) Yan, R. X.; Gargas, D.; Yang, P. D. *Nat. Photonics* **2009**, *3* (10), 569–576.

(8) Yang, P. D.; Yan, R. X.; Fardy, M. *Nano Lett.* **2010**, *10* (5), 1529–1536.

(9) Dick, K. A.; Deppert, K.; Larsson, M. W.; Martensson, T.; Seifert, W.; Wallenberg, L. R.; Samuelson, L. *Nat. Mater.* **2004**, *3* (6), 380–384.

(10) Fan, Z. Y.; Razavi, H.; Do, J. W.; Moriwaki, A.; Ergen, O.; Chueh, Y. L.; Leu, P. W.; Ho, J. C.; Takahashi, T.; Reichertz, L. A.; Neale, S.; Yu, K.; Wu, M.; Ager, J. W.; Javey, A. *Nat. Mater.* **2009**, *8* (8), 648–653.

(11) Fan, Z. Y.; Ruebusch, D. J.; Rathore, A. A.; Kapadia, R.; Ergen, O.; Leu, P. W.; Javey, A. *Nano Res.* **2009**, *2* (11), 829–843.

(12) Garnett, E.; Yang, P. D. *Nano Lett.* **2010**, *10* (3), 1082–1087.

(13) Ahn, J. H.; Kim, H. S.; Lee, K. J.; Jeon, S.; Kang, S. J.; Sun, Y. G.; Nuzzo, R. G.; Rogers, J. A. *Science* **2006**, *314* (5806), 1754–1757.

(14) Javey, A.; Nam, S.; Friedman, R. S.; Yan, H.; Lieber, C. M. *Nano Lett.* **2007**, *7* (3), 773–777.

(15) Nam, S.; Jiang, X. C.; Xiong, Q. H.; Ham, D.; Lieber, C. M. *Proc. Natl. Acad. Sci. U.S.A.* **2009**, *106* (50), 21035–21038.

(16) Adachi, M.; Murata, Y.; Takao, J.; Jiu, J. T.; Sakamoto, M.; Wang, F. M. *J. Am. Chem. Soc.* **2004**, *126* (45), 14943–14949.

(17) Briseno, A. L.; Holcombe, T. W.; Boukai, A. I.; Garnett, E. C.; Shelton, S. W.; Frechet, J. J. M.; Yang, P. D. *Nano Lett.* **2010**, *10* (1), 334–340.

(18) Chen, H. M.; Chen, C. K.; Chang, Y. C.; Tsai, C. W.; Liu, R. S.; Hu, S. F.; Chang, W. S.; Chen, K. H. *Angew. Chem., Int. Ed.* **2010**, *49* (34), 5966–5969.

(19) Jiu, J. T.; Isoda, S.; Wang, F. M.; Adachi, M. *J. Phys. Chem. B* **2006**, *110* (5), 2087–2092.

(20) Law, M.; Greene, L. E.; Johnson, J. C.; Saykally, R.; Yang, P. D. *Nat. Mater.* **2005**, *4* (6), 455–459.

(21) Liu, J. W.; Kuo, Y. T.; Klabunde, K. J.; Rochford, C.; Wu, J.; Li, J. *ACS Appl. Mater. Interfaces* **2009**, *1* (8), 1645–1649.

(22) Liu, B.; Aydil, E. S. *J. Am. Chem. Soc.* **2009**, *131* (11), 3985–3990.

(23) Czaban, J. A.; Thompson, D. A.; LaPierre, R. R. *Nano Lett.* **2009**, *9* (1), 148–154.

(24) Garnett, E. C.; Yang, P. D. *J. Am. Chem. Soc.* **2008**, *130* (29), 9224–9225.

(25) Greene, L. E.; Law, M.; Yuhas, B. D.; Yang, P. D. *J. Phys. Chem. C* **2007**, *111* (50), 18451–18456.

(26) Hwang, Y. J.; Boukai, A.; Yang, P. D. *Nano Lett.* **2009**, *9* (1), 410–415.

(27) Law, M.; Greene, L. E.; Radenovic, A.; Kuykendall, T.; Liphardt, J.; Yang, P. D. *J. Phys. Chem. B* **2006**, *110* (45), 22652–22663.

(28) Park, K.; Zhang, Q. F.; Garcia, B. B.; Zhou, X. Y.; Jeong, Y. H.; Cao, G. Z. *Adv. Mater.* **2010**, *22* (21), 2329–2332.

(29) Morin, S. A.; Bierman, M. J.; Tong, J.; Jin, S. *Science* **2010**, *328* (5977), 476–480.

(30) Wu, Y. Y.; Yang, P. D. *J. Am. Chem. Soc.* **2001**, *123* (13), 3165–3166.

(31) George, S. M. *Chem. Rev.* **2010**, *110* (1), 111–131.

(32) Knez, M.; Niesch, K.; Niinisto, L. *Adv. Mater.* **2007**, *19* (21), 3425–3438.

(33) Puurunen, R. L. *J. Appl. Phys.* **2005**, *97* (12), No. 121302.

(34) Ritala, M.; Leskela, M. *Nanotechnology* **1999**, *10* (1), 19–24.

(35) Groner, M. D.; Fabreguette, F. H.; Elam, J. W.; George, S. M. *Chem. Mater.* **2004**, *16* (4), 639–645.

(36) Ritala, M.; Kukli, K.; Rahtu, A.; Raisanen, P. I.; Leskela, M.; Sajavaara, T.; Keinonen, J. *Science* **2000**, *288* (5464), 319–321.

(37) Yang, R. B.; Zakharov, N.; Moutanabbir, O.; Scheerschmidt, K.; Wu, L. M.; Gosele, U.; Bachmann, J.; Nielsch, K. *J. Am. Chem. Soc.* **2010**, *132* (22), 7592–7594.

(38) Armstrong, A. R.; Armstrong, G.; Canales, J.; Garcia, R.; Bruce, P. G. *Adv. Mater.* **2005**, *17* (7), 862–865.

(39) Bach, U.; Lupo, D.; Comte, P.; Moser, J. E.; Weissortel, F.; Salbeck, J.; Spreitzer, H.; Gratzel, M. *Nature* **1998**, *395* (6702), 583–585.

(40) Bavykin, D. V.; Friedrich, J. M.; Walsh, F. C. *Adv. Mater.* **2006**, *18* (21), 2807–2824.

(41) Bruce, P. G.; Scrosati, B.; Tarascon, J. M. *Angew. Chem., Int. Ed.* **2008**, *47* (16), 2930–2946.

(42) Gratzel, M. *Nature* **2001**, *414* (6861), 338–344.

(43) Yang, H. G.; Sun, C. H.; Qiao, S. Z.; Zou, J.; Liu, G.; Smith, S. C.; Cheng, H. M.; Lu, G. Q. *Nature* **2008**, *453* (7195), 638–641.

(44) Zuruzi, A. S.; Kolmakov, A.; MacDonald, N. C.; Moskovits, M. *Appl. Phys. Lett.* **2006**, *88* (10), 102904.

(45) Kemell, M.; Harkonen, E.; Pore, V.; Ritala, M.; Leskela, M. *Nanotechnology* **2010**, *21* (3), No. 035301.

(46) Aarik, J.; Aidla, A.; Uustare, T.; Sammelselg, V. *J. Cryst. Growth* **1995**, *148* (3), 268–275.

(47) Alekhin, A. P.; Lapushkin, G. I.; Markeev, A. M.; Sigarev, A. A.; Toknova, V. F. *J. Surf. Invest. X-Ray Synchrotron Neutron Tech.* **2010**, *4* (3), 379–383.

(48) King, D. M.; Du, X. H.; Cavanagh, A. S.; Weimer, A. *Nanotechnology* **2008**, *19* (44), No. 445401.

(49) Park, M. H.; Jang, Y. J.; Sung-Suh, H. M.; Sung, M. M. *Langmuir* **2004**, *20* (6), 2257–2260.

(50) Liang, X. H.; King, D. M.; Li, P.; Weimer, A. W. *J. Am. Ceram. Soc.* **2009**, *92* (3), 649–654.

(51) Barnard, A. S.; Curtiss, L. A. *Nano Lett.* **2005**, *5* (7), 1261–1266.

(52) Barnard, A. S.; Zapol, P. *J. Phys. Chem. B* **2004**, *108* (48), 18435–18440.

(53) Polleux, J.; Pinna, N.; Antonietti, M.; Niederberger, M. *Adv. Mater.* **2004**, *16* (5), 436–439.

(54) Wu, J. M.; Shih, H. C.; Wu, W. T.; Tseng, Y. K.; Chen, I. C. *J. Cryst. Growth* **2005**, *281* (2−4), 384–390.

(55) Zhang, Y. X.; Li, G. H.; Jin, Y. X.; Zhang, Y.; Zhang, J.; Zhang, L. D. *Chem. Phys. Lett.* **2002**, *365* (3−4), 300–304.

(56) These numbers were obtained from the bulk values of anatase TiO_2 crystal. Due to surface strain, lattice constants on the crystal surface may be smaller than the bulk values. This effect is typically more significant along the depth of the crystal but shows less impact to in-plane lattices. Thus, based on the geometry, the distance between near neighbors may be further reduced, while the distance between far neighbors may be less affected.